Supporting Information

for

"Photothermal Microscopy of Non-luminescent Single Particles Enabled by Optical Microresonators"

*Kevin D. Heylman, Kassandra A. Knapper, Randall H. Goldsmith.**

Department of Chemistry, University of Wisconsin-Madison, 1101 University Avenue, Madison, Wisconsin 53706, United States

Table of Contents:

1: Materials and Methods

Coupling to Optical Microresonators

Toroidal microresonators are fabricated following the original literature procedure[1] with one modification. The XeF_2 dry chemical etch is replaced with an SF_6/Ar plasma etch[2] on an STS Multiplex ICP. The major diameter of the finished toroidal microresonators is 45-50 μm. This size was chosen to maximize the ratio of the Q-factor to the mode volume;[3] this ratio determines the sensitivity of the microresonator to resonance shifts. Tapered optical fibers are used to efficiently couple into microresonators.[1] Tapered fibers are fabricated by heating and pulling SMF-28e+ fiber until single-mode, air-guided propagation is observed. Only tapered fibers that are nearly adiabatic (>90 % transmission) are used in experiments. Two microscopes (Nikon FN1 and Navitar Ultrazoom) are used to align the tapered fiber and the toroidal microresonator. A long-travel piezostage (Attocube ECS 3030) and a micrometer stage (Thorlabs PT3) allow for the tapered fiber and microresonator to be coaligned at the center of the field of view of the high NA objective (Nikon CFI 60x, 0.95 air), which is used to deliver excitation light. Resonances are probed with a narrow-linewidth external-cavity tunable diode laser (New Focus TLB-6728, 1520-1570 nm) and the transmission through the optical fiber is detected on a photodiode (Thorlabs S154C). Coupled power is kept low (~ 250 nW) to avoid thermal broadening of the resonance.[4]

Delivering Excitation Light

The target nano-object is optically excited by a near-diffraction-limited excitation beam delivered by the high-NA objective. A fixed-wavelength diode laser (Blue Sky Research, 640 nm) is used at low power (0.44 mW) for optical excitation. The output of the laser is passed through a polarizer and a λ/2-plate to allow for tuning of the linear polarization angle at the target. A polarization extinction ratio of 116:1 was measured right before the objective using a Glan-laser polarizer, demonstrating that the excitation

beam is almost completely linearly polarized. A galvanically-controlled (Newport TRA12CC), gimbal-mounted mirror and a pair of relay lenses are used to control the angle at which the beam is incident upon the back focal plane of the objective. Angular variation in incidence upon the back focal plane translates into spatial shift of the beam at the sample plane with no angular shift. The transmitted intensity through the objective is measured across the full range of the field of view, which is larger than the microresonator, and found to vary by ≤ 5 %.

Photothermal Mapping

Photothermal maps are taken by raster-scanning the focused excitation beam across the toroid while measuring the relative wavelength of the toroid resonance. Initially coarse maps are taken of entire microresonators in order to locate individual nano-objects (see Figure 1d). Bright pixels correspond to individual absorbers. Photothermal signal is also observed from the silicon support pillar, although it varies slowly enough to appear as a nearly constant background shift on high-resolution maps. High-resolution maps are taken after optimizing the polarization angle and focus of the excitation beam for maximum resonance shift. At every pixel the resonance shift is measured with the excitation beam turned on and off, to account for possible drift of the probe wavelength. A custom Labview program is used to synchronize scanning of the excitation beam, resonance shift measurement, and control of the excitation beam position. Signal averaging is not necessary for sufficiently bright objects (such as multi-walled carbon nanotubes and carbon nanofibers). In this work, five successive scans across the toroid resonance were used. The length of time to measure the resonance shift at each pixel (~ 600 ms) is currently limited by the control software, not by the physics of thermal equilibration (~ 0.25 ms)[5] or the maximum scan rate of the probe laser (~ 1 ms). The excitation beam is scanned in 250 nm steps over a 6 µm x 6 µm range, centered on the target. Polarization dependence is measured by tuning the angle of the λ/2-plate while recording the observed resonance shift on the center of the nano-object.

Finite-element Simulations

Photothermally-induced resonance shift in toroidal microresonators is modeled using COMSOL Multiphysics 4.3a, a finite-element solver. Equilibrium temperature distribution is simulated with a three-dimensional model of a toroid, using physical dimensions extracted from SEM images of the toroids used in these experiments. Single multi-walled nanotubes are modelled as cylinders with dimensions and locations extracted from SEM images. Nanotubes are treated as boundary heat sources. Steady-state solutions to the conductive heat equation are solved for using a software-defined extra-fine mesh. Both radiative and convective heat transfer were found to have negligible (< 0.1%) effect on the calculated temperature rise. From the heat transfer solution, two-dimensional slices of the mode area of the toroid are taken at regularly-spaced azimuthal intervals (5°) and overlapped with the known mode profile of the toroidal microresonator.[6] The resulting resonance shift is averaged over every azimuthal position, and the simulated resonance shift is compared to the experimentally-measured resonance shift. The inputted heat flow required from the nanotube is adjusted until the simulated resonance shift matches the measured shift. Knowledge of this heat flow is necessary for calculating the per-atom absorption cross-section, as described in section 4 of the Supporting Information.

2: Additional SEMs

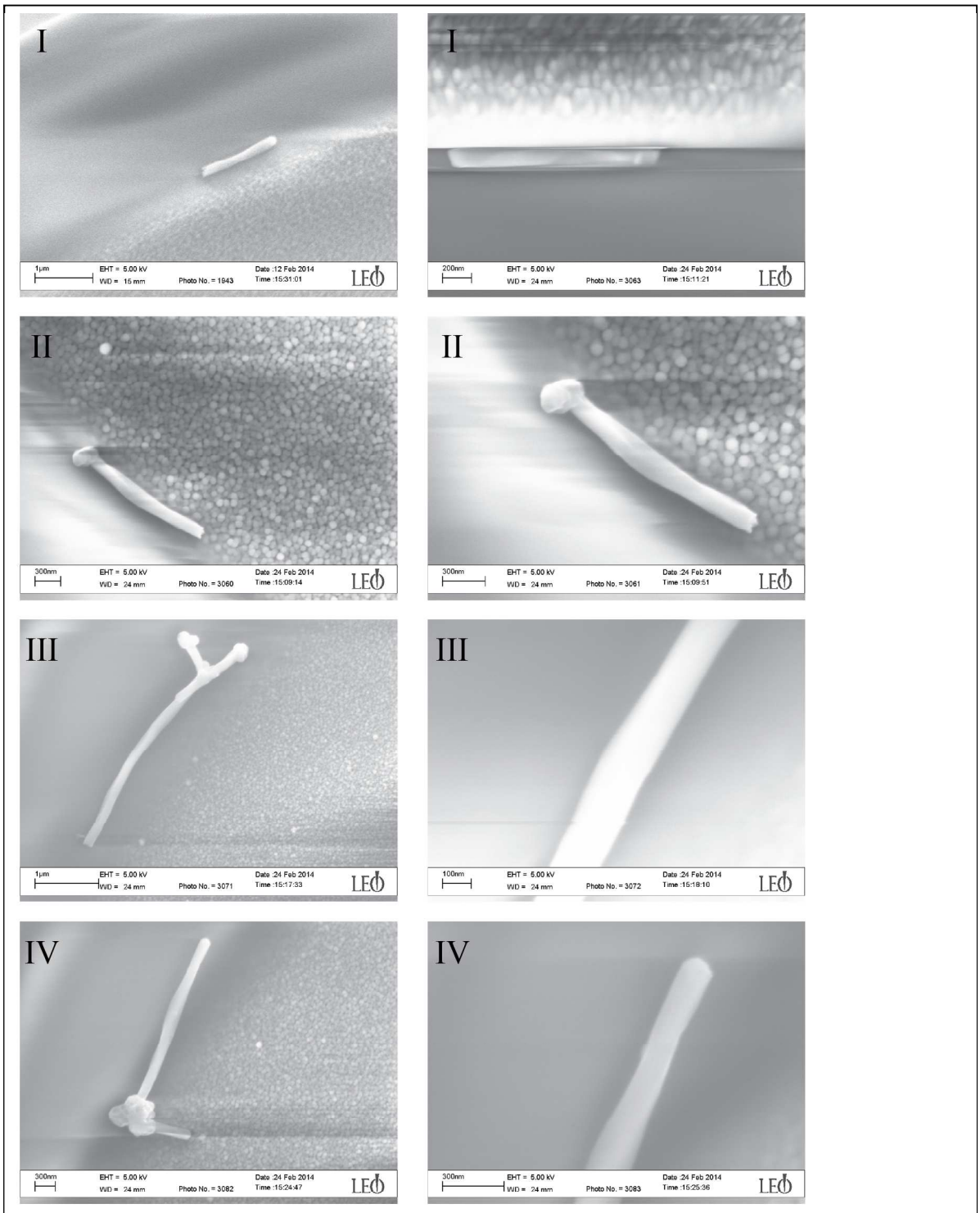

Figure S1. Additional SEMs of Nanotubes I-IV (from Figure 3). The relative orientation of the nanotube varies owing to different mounting conditions in the SEM. These micrographs were used to measure the length and diameter of each nanotube.

3: Noise and Background

The resonance shift under pump laser illumination is calculated by measuring the microresonator's resonance wavelength with the pump laser on and off and taking the difference. Dominant sources of noise include wavelength fluctuations in the probe laser, thermally-induced fluctuations in the resonator's intrinsic resonance wavelength, and fluctuations in the strength of the coupling, largely caused by fluctuations in the taper-resonator spacing. However, the nanotubes are cleanly resolved versus the background and noise. As an example, consider the photothermal map in Figure 3, Nanotube I. To estimate the background signal, we can look at pixels that are distant from the nanotube feature at the center. The mean for the first column on the left is a shift of 524 +/- 43 fm. The rightmost column is 695 +/- 79 fm. The rightmost column has a higher background because it is closer to the center of the toroid, and the silicon absorption is more effectively conducted to the toroidal rim.[5] The background at column 13 (crossing the center of the nanotube) is estimated to be 600 +/- 60 fm (from pixels significantly below and above the feature). The peak signal from the nanotube gives a shift of 14,110 fm. These values yield a signal-background ratio of 14,110 fm / 600 fm = 24, and a signal-noise ratio of 230.

4: Calculating the Fraction of Carbon Atoms Absorbing

Nanotubes are modelled as cylinders, with length and diameter assigned by measurements extracted from SEM images. The fraction of atoms excited can be calculated by taking an overlap integral between two functions, one defining the spatial distribution of atoms in the nanotube and the other defining the Gaussian shape of the excitation beam. The function defining the number of atoms is constructed by multiplying the known bulk atom density ($\rho \times N_a/M$) by the position-dependent height, $h(x,y)$, and a differential area, dxdy. The maximum value of the $h(x,y)$ function is the diameter of the nanotube. For the second function, the pump beam spot is modelled as a symmetric 2-dimensional Gaussian function of width 780 nm. In actuality, the excitation volume is slightly asymmetric (750 nm x 810 nm, based on measurements of the microscope's point-spread-function). However, replacing the asymmetric

Gaussian with a symmetric Gaussian whose width was equal to the mean of the two values changed the calculated per-atom absorption cross-section by less than 4 %. The total fraction of atoms absorbing light (β) is the 2-dimensional integral of the product of these two functions divided by the total number of atoms in the nanotube,

$$\beta = \frac{\iint dxdy[\, h(x,y) * \rho * \frac{N_a}{M}] * [\exp\left(-\frac{(x-x_0)^2}{0.5 * \sigma_x^2} - \frac{(y-y_0)^2}{0.5 * \sigma_y^2}\right)]}{\iint dxdy[\, h(x,y) * \rho * \frac{N_a}{M}]}$$

where x0 and y0 define the beam center position, σ_x^2 and σ_x^2 define the beam width for the general case of a nonsymmetric 2-dimensional Gaussian,and the remaining parameters are defined as for equation 1. All calculations in this work treat $\sigma_x^2 = \sigma_x^2$.

Two critical experimental parameters that are inputs into the above calculation are the carbon nanotube length and diameter. Figure S2 shows the effect of small variations in these parameters on the calculated per carbon absorption cross-section in order to gauge how slight measurement errors can influence our calculation. Figure S2a shows the effect of varying the length of the nanotube. Even for the shortest nanotube of the four investigated, at 1.4 μm in length, the farthest ends of the nanotubes are much larger than the width of the excitation beam. In other words, nanotubes of the same diameter but different length should have essentially identical maximum photothermal signal as long as they are > 1 μm in length. Consequently, Figure S2a shows that there is little effect on the per atom cross-section from errors in length determination, though nanotubes of different length can still be distinguished by the different apparent length in the photothermal maps. Figure S2b shows the effect of variations in the nanotube diameter on the per atom absorption cross-section. In this case, the nanotube diameter does strongly affect the absorption cross-section per atom, by quadratically affecting the number of atoms in the nanotube per unit length. Consequently, the calculated absorption cross-section per atom at constant dissipated power varies inversely with the nanotube diameter. An uncertainty of 10 nm (a

reasonable upper limit considering the images in Figure S1) in the measured diameter corresponds to 11% uncertainty in the calculated absorption cross-section. This is likely the dominant contribution to the uncertainty in our per atom cross-section measurements.

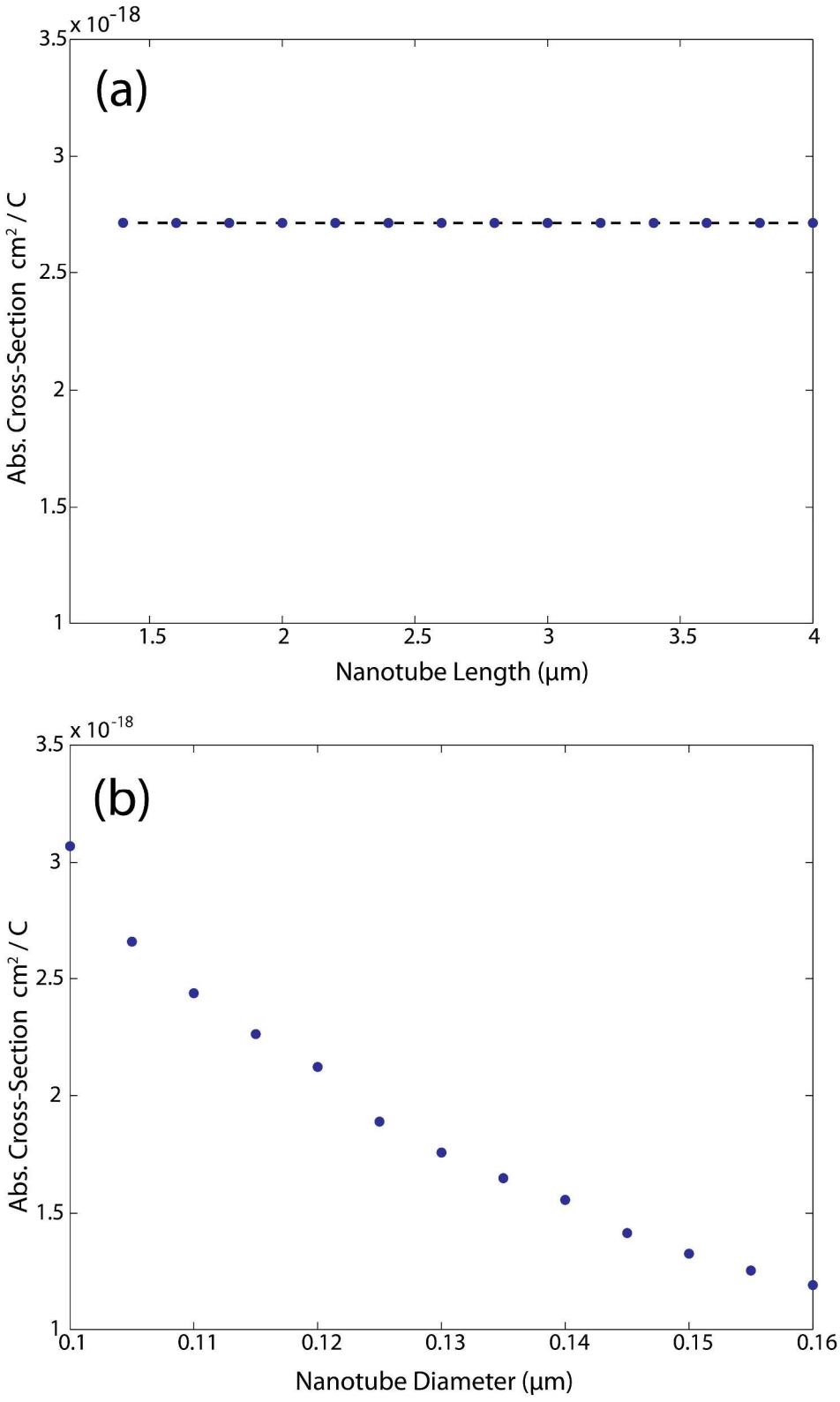

Figure S2. Effect of varying nanotube dimensions on calculated per-atom absorption cross-section. (a) Nanotube length dependence and (b) nanotube diameter dependence. A horizontal dashed line is present in (a) for emphasis.

5: Simulated Time Dependence

We explored the time to reach equilibrium shift via simulations. The simulated resonance shift as a function of time is plotted in Figure S3. Simulations in COMSOL are used to plot the temperature distribution at each time point (in this case Nanotube I is modelled), and the resonance shift of the toroid is calculated just as in the equilibrium calculation. Assuming only conductive heat transfer, thermal equilibration should follow a mono-exponential time dependence (this is the solution to the Helmholtz equation, which describes heat conduction). An exponential fit closely matches the simulated time dependence. The calculated 1/e rise time (154 μs) is similar to that experimentally measured for a bare toroid pumped at the center of the toroid (τ = 240 μs).[5] This agreement is not unexpected—in one experiment the heat is deposited at the rim of the toroid and must reach the center for equilibration, and in the other it is deposited at the center and must reach the rim of the toroid to affect the propagating mode.

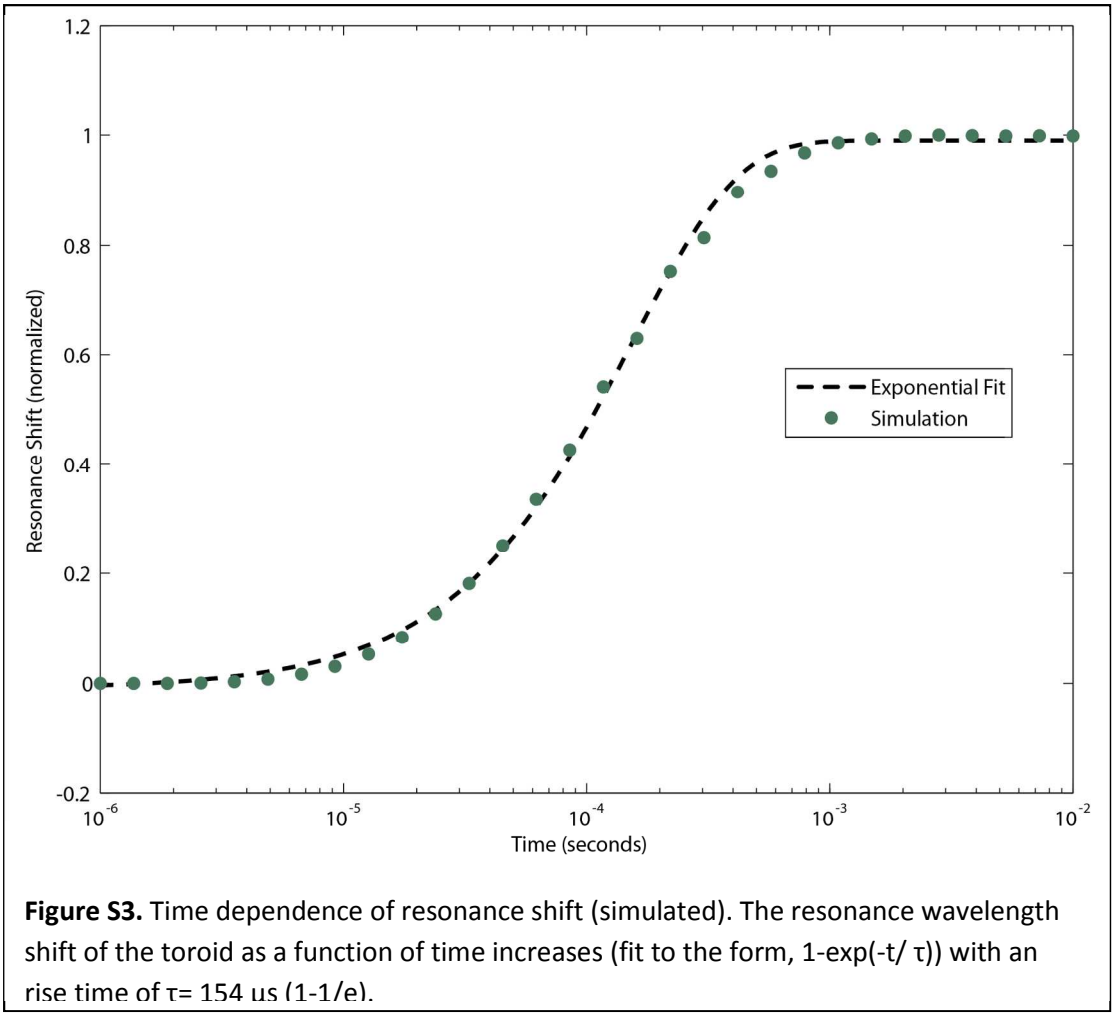

Figure S3. Time dependence of resonance shift (simulated). The resonance wavelength shift of the toroid as a function of time increases (fit to the form, 1-exp(-t/ τ)) with an rise time of τ= 154 μs (1-1/e).

6: Power Dependence

The power dependence of the photothermal signal was tested by varying the pump power incident on a nanotube. Figure S4 shows the observed highly linear trend, ranging from 0.14 mW to 1.71 mW of incident power.

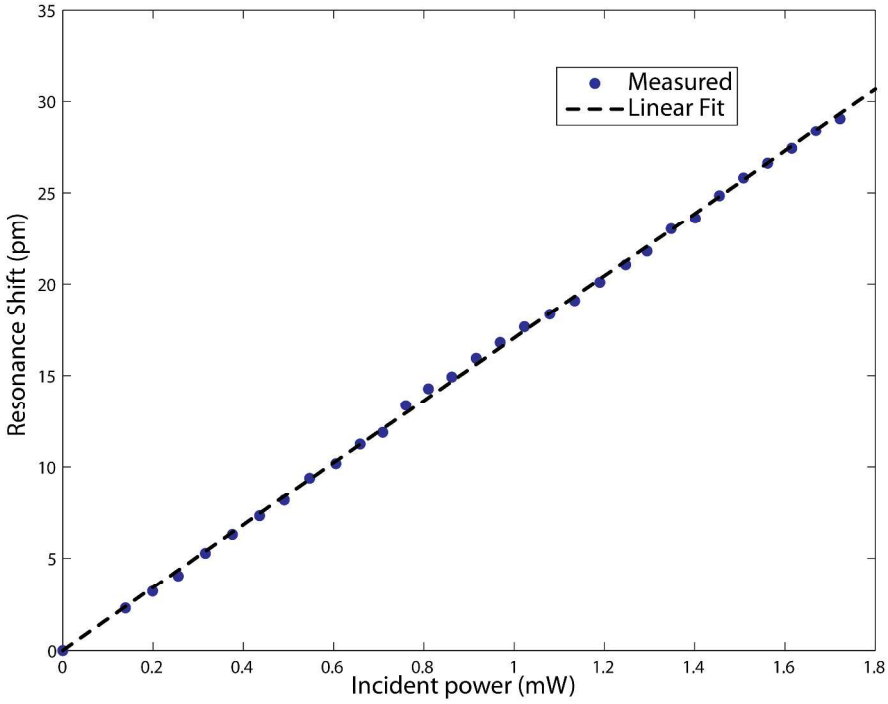

Figure S4. Power dependence of measured resonance shift. The measured resonance shift is linear over the order of magnitude investigated.

7: Polarization Dependence

The orientation of Nanotubes I-IV was assigned by inspection, and in all cases the direction of the long axis of the nanotube lay within 6° of the polarization direction of the pump beam where the maximum photothermal shift was achieved. Photothermal maps taken at crossed (90°) polarization indicate no change in morphology for straight nanotubes, merely a difference in photothermal signal, Figure S5. Photothermal maps taken on small groups of nanotubes reveal a difference in the relative photothermal intensity of different nanotubes as the polarization is rotated Figure S6.

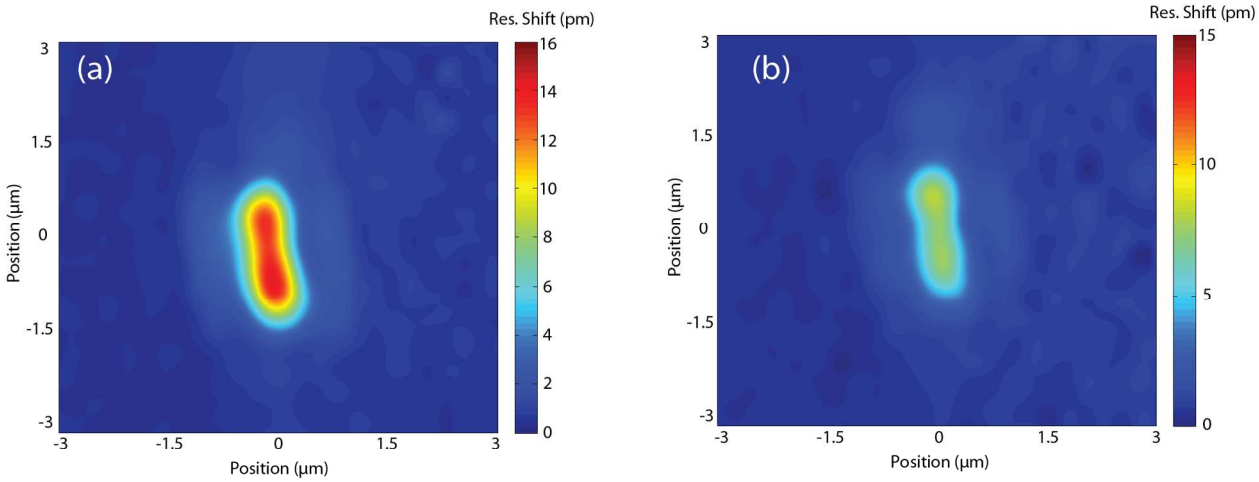

Figure S5. Photothermal maps with the pump beam polarization aligned parallel to the long axis (a) and perpendicular (b) for nanotube I in Figure 3.

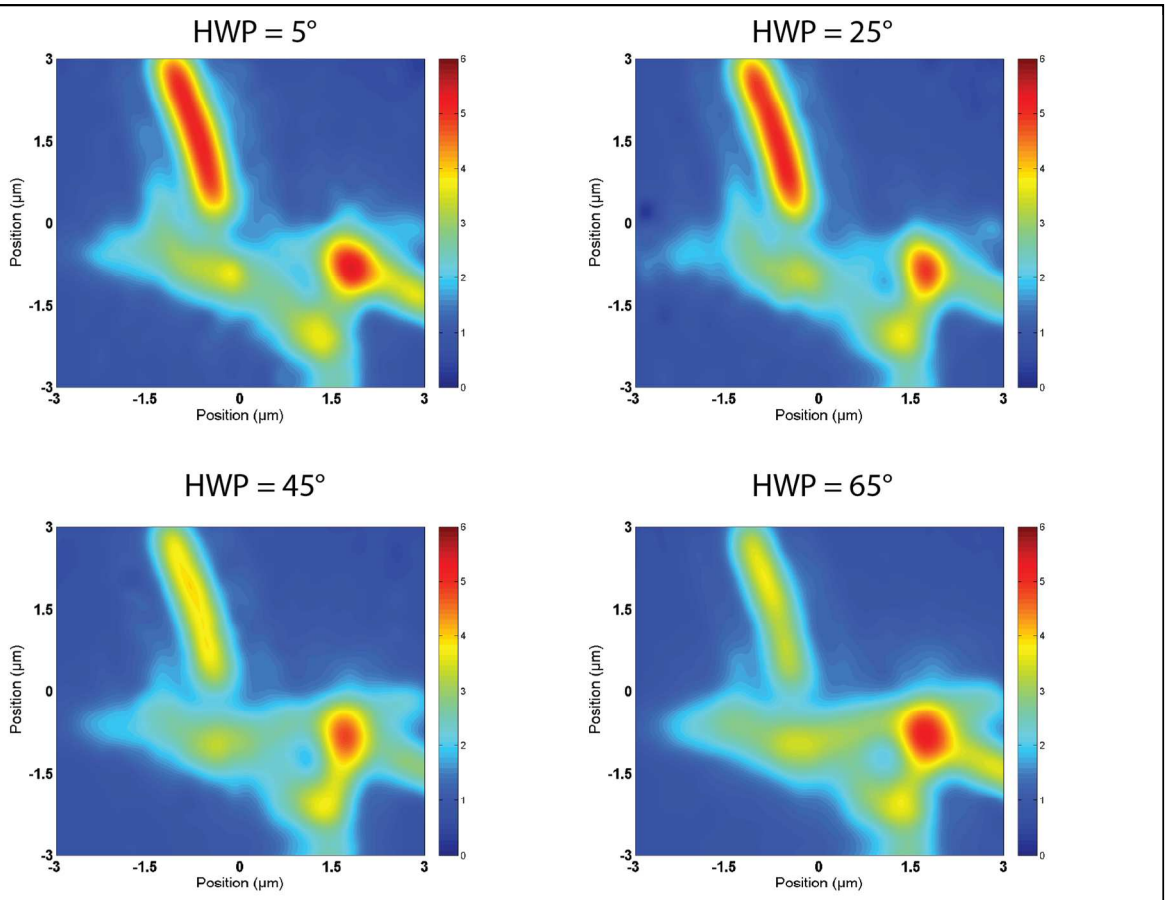

Figure S6. Polarization dependence of photothermal signal on a cluster of MWCNTs. As the polarization is rotated over 120°, the map changes morphology as different nanotubes brighten and dim.

8: Parameter Testing of COMSOL simulation

The effect of varying the smallest allowable element size in the tetrahedral meshing of the modeled microresonator-nanotube system was investigated. Figure S7 shows that large changes in mesh size have minimal (<0.5%) effect on calculated resonance shifts.

The effect of varying the distance between the nanotube and the surface of the resonator was also investigated. Figure S8 demonstrates that shifting the vertical position of the nanotube over tens of nanometers, either by raising it above the microresonator surface or by lowering it below the surface, also has a minimal effect (<0.5%) on the calculated resonance shift. One of the conclusions that can be drawn from this result concerns that magnitude of interfacial thermal resistance. Several groups have endeavored[7-11] to experimentally determine the interfacial thermal resistance between a nanotube and various surfaces, with a large range of values observed. While such an interfacial resistance was not explicitly included in our calculation, the opening up of a highly insulating thin air layer between the tube and the resonator surface can indirectly probe this possibility. This situation has little effect on the resonance shift, likely due to the extremely small heat capacity of the nanotube relative to the microresonator. Since the inclusion of this layer had only extremely minor influence on the microresonator equilibrium temperature distribution and resulting photothermal shift, we infer that our not explicitly including an interfacial thermal resistance has little influence on the calculation and is a reasonable approximation.

9: Uncertainty in the thermal conductivity of MWCNTs

The simulation is also highly insensitive to the thermal conductivity of the nanotube. Various reports have placed this conductivity in the range of 3000 W/m*K to 42 W/m*K, depending on the measurement method and the concentration of defects in the MWCNT.[12-17] Changing the conductivity in the model from 3000 to 3 W/m*K changed the predicted resonance shift by only 1 part in 10,000. Therefore, we conclude that the wide range of possible values for the thermal conductivity of the nanotubes used in this study does not affect the accuracy of the calculation.

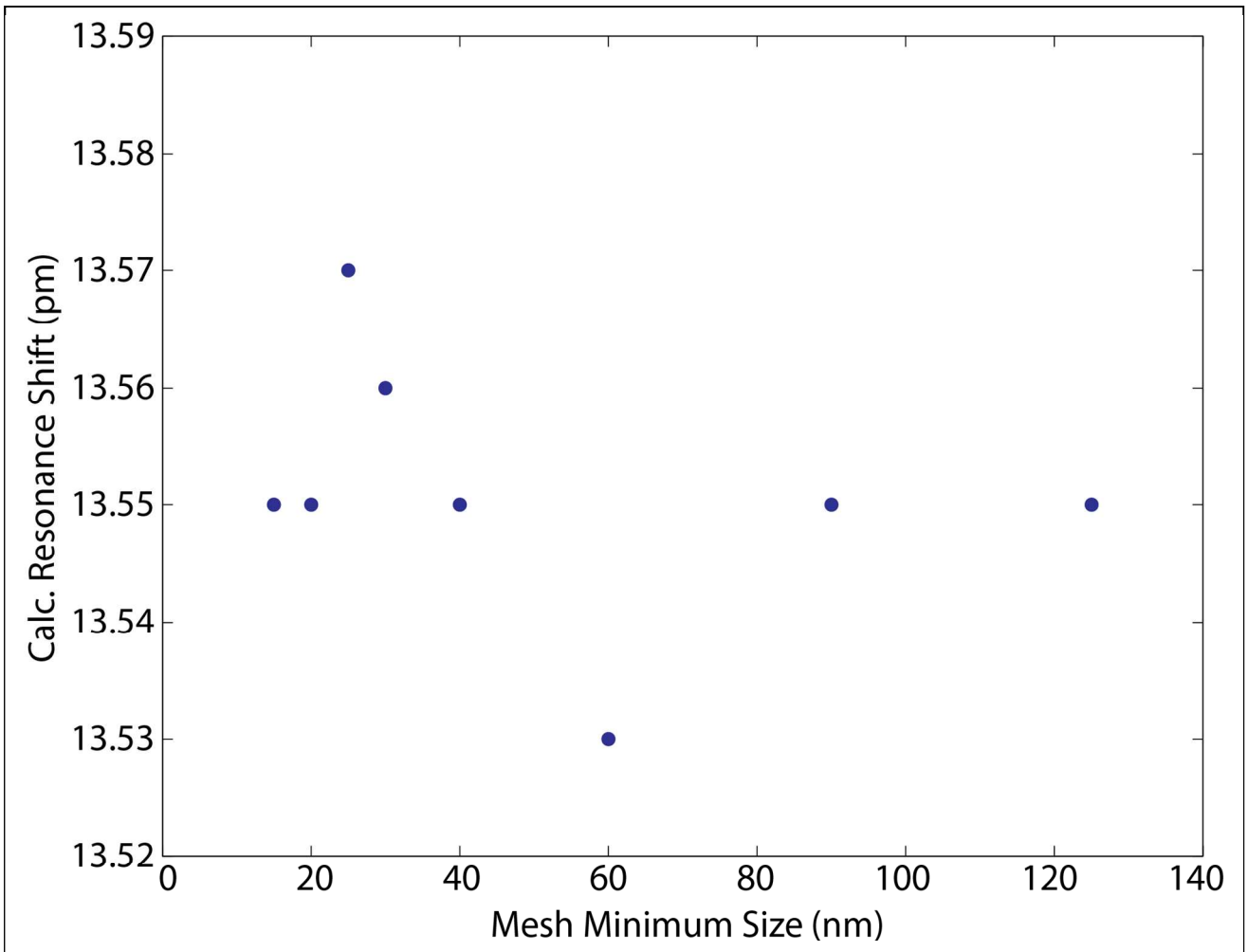

Figure S7. Effect of meshing size on the simulation's accuracy. The minimum allowed edge length for a tetrahedral meshing of the nanotube-decorated toroidal microresonator is varied from 15 nm to 125 nm. No systematic effect on the calculated resonance shift under pump beam illumination is found.

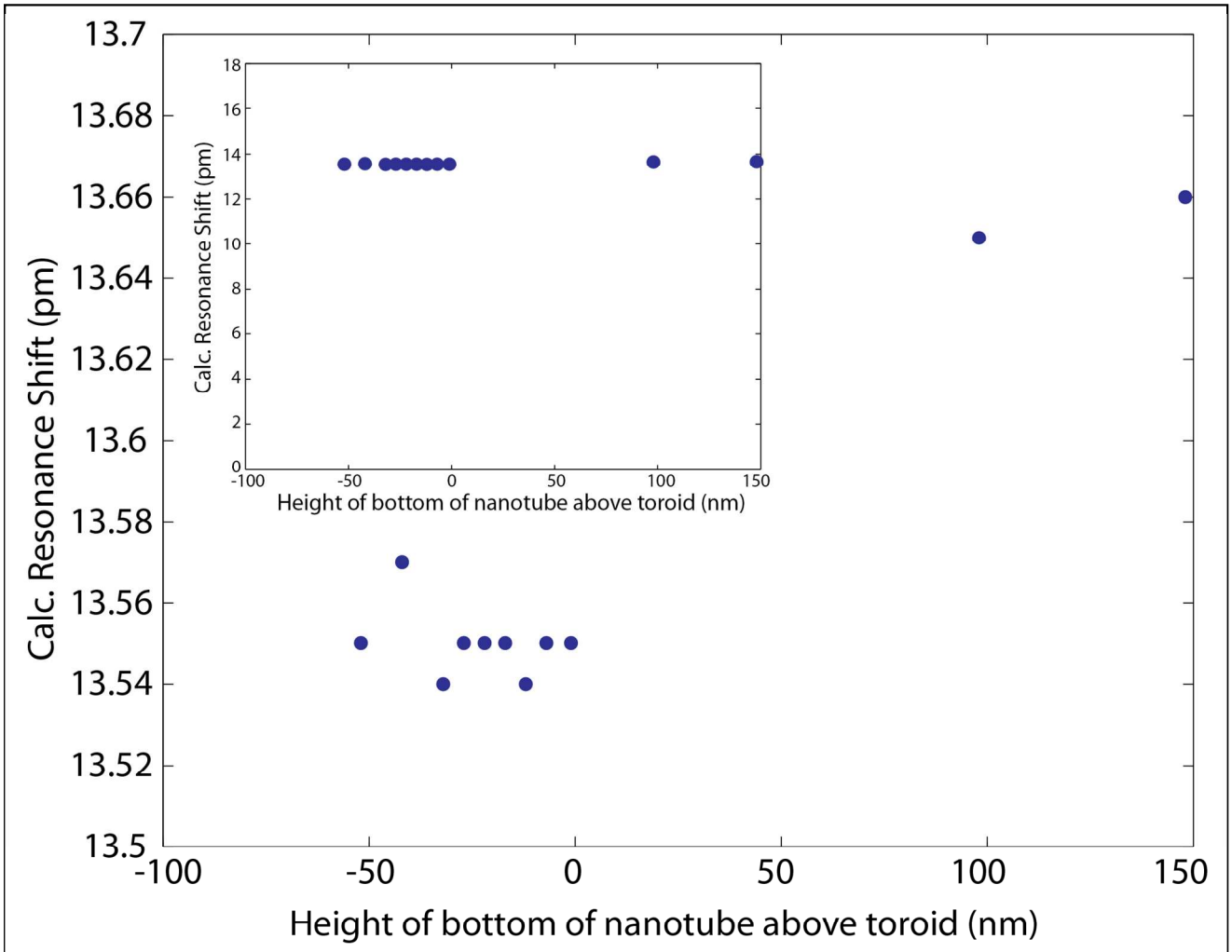

Figure S8. Effect of nanotube-microresonator interfacial contact distance on calculated resonance shift. The distance between the bottom edge of the nanotube and the top of the silica surface of the microresonator is varied and the effect on the calculated resonance shift measured. The nanotube is 52 nm in radius, and so the nanotube is 50% "immersed" in the resonator at x =-52 nm; conversely, at x = 150 nm the nanotube is suspended in air more than 1 diameter above the surface. Larger, more positive values along the x-axis correspond to less contact area between the nanotube and the resonator. No significant trend is observed, implying that this simulation is tolerant of large uncertainty in the nanotube-silica interfacial thermal resistance. **Inset:** Calculated resonance shift with the entire axis range, demonstrating that the variations observed in the main figure are negligible compared to the total resonance shift.

References

1. Armani, D. K.; Kippenberg, T. J.; Spillane, S. M.; Vahala, K. J. Ultra-high-Q toroid microcavity on a chip. *Nature* **2003,** *421,* 925-928.
2. Jager, J. B.; Calvo, V.; Delamadeleine, E.; Hadji, E.; Noe, P.; Ricart, T.; Bucci, D.; Morand, A. High-Q silica microcavities on a chip: From microtoroid to microsphere. *Appl. Phys. Lett.* **2011,** *99,* 181123.
3. Kippenberg, T. J.; Spillane, S. M.; Vahala, K. J. Demonstration of ultra-high-Q small mode volume toroid microcavities on a chip. *Appl. Phys. Lett.* **2004,** *85,* 6113-6115.
4. Rokhsari, H.; Spillane, S. M.; Vahala, K. J. Loss characterization in microcavities using the thermal bistability effect. *Appl. Phys. Lett.* **2004,** *85,* 3029-3031.
5. Heylman, K. D.; Goldsmith, R. H. Photothermal mapping and free-space laser tuning of toroidal optical microcavities. *Appl. Phys. Lett.* **2013,** *103,* 211116.
6. Oxborrow, M. Traceable 2-D finite-element simulation of the whispering-gallery modes of axisymmetric electromagnetic resonators. *IEEE Trans. Microwave Theory Tech* **2007,** *55,* 1209-1218.
7. Wang, D.; Carlson, M. T.; Richardson, H. H. Absorption Cross Section and Interfacial Thermal Conductance from an Individual Optically Excited Single-Walled Carbon Nanotube. *ACS Nano* **2011,** *5,* 7391-7396.
8. Kim, P.; Shi, L.; Majumdar, A.; McEuen, P. L. Thermal transport measurements of individual multiwalled nanotubes. *Phys. Rev. Lett.* **2001,** *87,* 215502.
9. Maune, H.; Chiu, H. Y.; Bockrath, M. Thermal resistance of the nanoscale constrictions between carbon nanotubes and solid substrates. *Appl. Phys. Lett.* **2006,** *89,* 013109.
10. Shi, L.; Zhou, J. H.; Kim, P.; Bachtold, A.; Majumdar, A.; McEuen, P. L. Thermal probing of energy dissipation in current-carrying carbon nanotubes. *J. Appl. Phys.* **2009,** *105,* 104306.
11. Pop, E. The role of electrical and thermal contact resistance for Joule breakdown of single-wall carbon nanotubes. *Nanotechnology* **2008,** *19,* 295202.
12. Pettes, M. T.; Shi, L. Thermal and Structural Characterizations of Individual Single-, Double-, and Multi-Walled Carbon Nanotubes. *Adv Funct Mater* **2009,** *19,* 3918-3925.
13. Kim, P.; Shi, L.; Majumdar, A.; McEuen, P. L. Thermal transport measurements of individual multiwalled nanotubes. *Phys. Rev. Lett.* **2001,** *87*.
14. Samani, M. K.; Khosravian, N.; Chen, G. C. K.; Shakerzadeh, M.; Baillargeat, D.; Tay, B. K. Thermal conductivity of individual multiwalled carbon nanotubes. *Int J Therm Sci* **2012,** *62,* 40-43.
15. Choi, T. Y.; Poulikakos, D.; Tharian, J.; Sennhauser, U. Measurement of thermal conductivity of individual multiwalled carbon nanotubes by the 3-omega method. *Appl. Phys. Lett.* **2005,** *87,* 013108.
16. Choi, T. Y.; Poulikakos, D.; Tharian, J.; Sennhauser, U. Measurement of the thermal conductivity of individual carbon nanotubes by the four-point three-omega method. *Nano Lett.* **2006,** *6,* 1589-1593.
17. Yang, J. K.; Yang, Y.; Waltermire, S. W.; Gutu, T.; Zinn, A. A.; Xu, T. T.; Chen, Y. F.; Li, D. Y. Measurement of the Intrinsic Thermal Conductivity of a Multiwalled Carbon Nanotube and Its Contact Thermal Resistance with the Substrate. *Small* **2011,** *7,* 2334-2340.